

Supplement to: Regional centroid MT inversion of small to moderate earthquakes in the Alps using the dense AlpArray seismic network: challenges and seismotectonic insights

G.M. Petersen, S. Cesca, S. Heimann, P. Niemz, T. Dahm, D. Kühn, J. Kummerow, T. Plenefisch and the AlpArray working group

The supplementary material contains two tables with moment tensor solutions, and documents additional analysis steps with three figures to complement the main manuscript.

1. List of centroid moment tensor solutions

Centroid moment tensor solutions and their uncertainties are provided in two tables *Alps_2016-2019_CMT-best-solutions_Petersen.csv* and *Alps_2016-2019_CMT-statistics-solutions_Petersen.csv*. The first table provides the best solution for each event. *Best* refers to the single solution which best fits the input data. The second table contains mean, standard deviation and median of each inversion parameter, obtained from the ten best solutions of all bootstrap (BS) chains (see main text). At least 100 BS chains were used in each inversion.

2. Moment tensor inversion using waveform envelopes

In additional tests of the input data type, we use smoothed envelopes of the displacement waveforms in combination with full waveforms as input data to the moment tensor inversion. For small events with $M_w \leq 3.3$, often only the waveforms of the closest stations (e.g. distance ≤ 70 km) can be fitted directly. By combining the time-domain full waveform input for close stations with the envelopes of waveforms of more distant stations, we attempt to study also those events, for which full waveforms alone do not provide stable results.

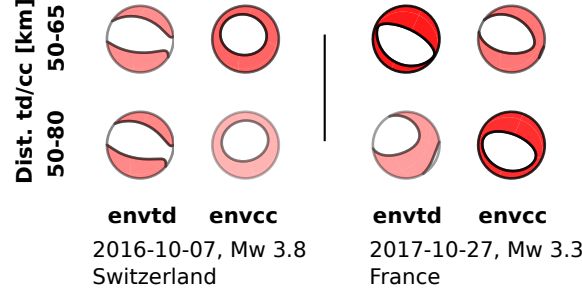


Figure S1: Exemplary testing of envelopes (*env*) in combination with time domain full waveforms (*td* or *cc*) of close stations as input data type (bandpass filtered between 0.02 and 0.07 Hz). *td* refers to sample-wise fitting of full-waveforms and *cc* to cross-correlation fitting of full waveforms. The y-axis shows the distance range in which time domain data was used. The envelopes are computed for a distance range of 30-160 km. (left) Event 2016-10-07, Mw 3.8, Switzerland. (right) Event 2017-10-27, Mw 3.3, France.

3. Stress inversion

We use an in-house developed stress inversion routine to study the stress field five sub-regions of the study area (Fig. S2). The inversion is based on the minimization of the seismic energy released on unfavourably oriented faults and provides the directions of maximum stress σ_1 , intermediate stress σ_2 and minimum stress σ_3 and the relative stress magnitude $R = (\sigma_1 - \sigma_2) / (\sigma_1 - \sigma_3)$ [Cesca et al., 2016]. Our results agree well with stress inversion results obtained with the method introduced by Gephart and Forsyth [1984]. Stress directions that are well resolved show similar orientations, while similar resolution problems occur in both methods.

In the Western Alps, the stress field is not homogeneous. While normal faulting events are dominant, which results in the observed sub-vertical σ_1 direction and the sub-horizontal σ_3 direction, the scatter of input data and consequently the uncertainties are large.

In the central Alps, close to Lake Garda, only few MTs are available. The high R value and the badly resolved direction of σ_3 observed for this region indicates that the intermediate stress σ_2 and the minimum stress σ_3 have similar magnitudes. Among the six MT solutions available for this area there are five thrust mechanisms and one strike-slip mechanism. The latter significantly disturbs the resolution of the σ_3 direction, but the maximum stress direction σ_1 is well resolved because all events have similar P axes.

We observe a rotation of the σ_1 direction between the Friuli area in the Eastern Alps and the Northern Dinarides from NNW-SSE to NNE-SSW. While thrust faulting mechanisms are dominant in the Friuli region, the horizontal σ_3 direction in the Northern Dinarides represents dominant strike-slip mechanisms.

The Apennines show two sub-regions: In the NE part thrust mechanisms are dominant, while in the central Apennines normal faulting events dominate. The boundary separating the two regions/classes of mechanisms was estimated using a support vector machine approach implemented in scikit learn [Pedregosa et al., 2011]. Two parameters are set to weight the complexity of the boundary against the penalty for wrong

classification.

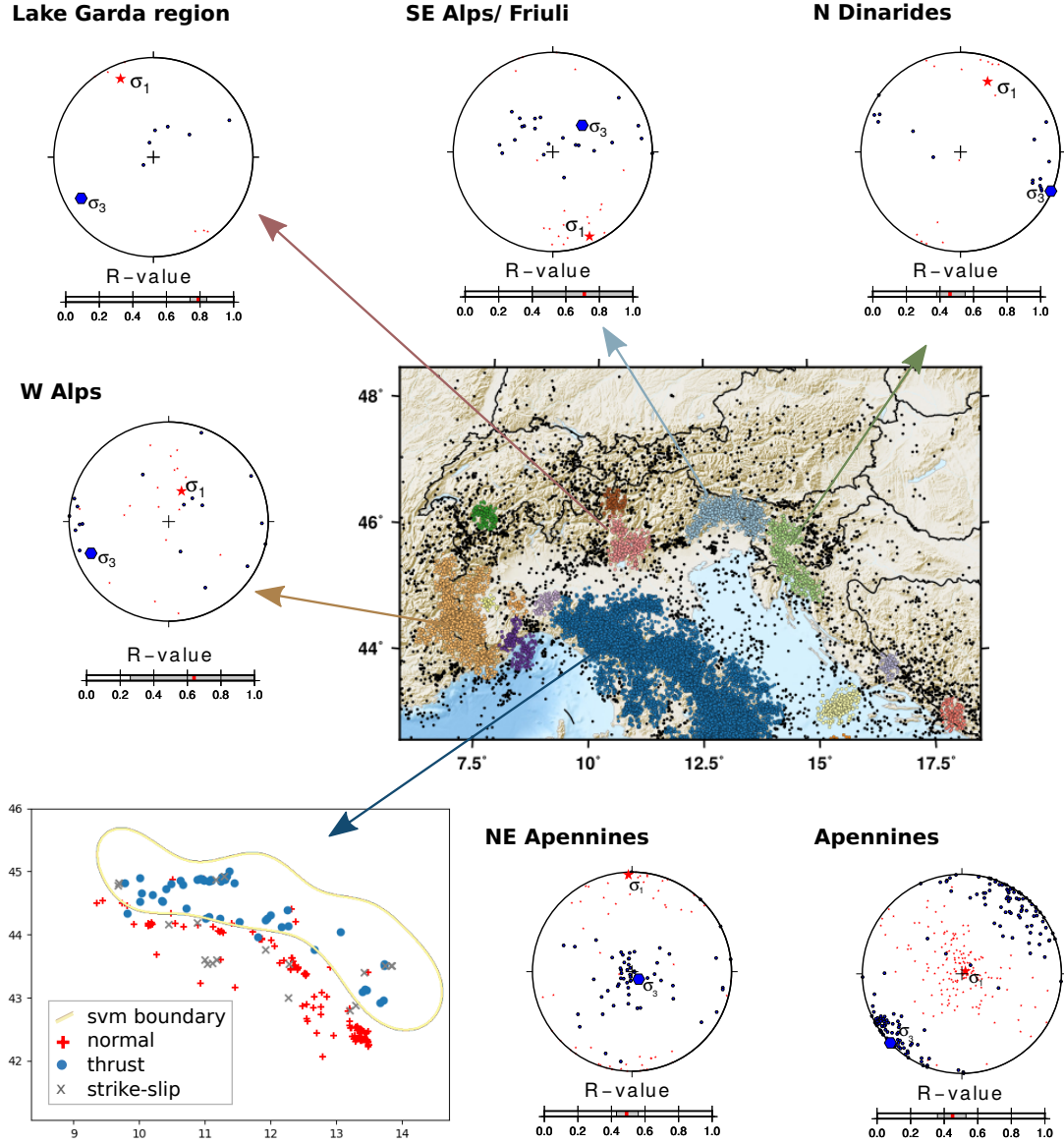


Figure S2: Stress inversion results from moment tensor solutions of five Alpine regions obtained with an in-house developed inversion code. The map indicates the location of the selected volumes. The lower left subplot depicts the division of the seismicity cluster in Apennines into two subregions. The orientations of the maximal (σ_1) and least (σ_3) compressive stress are projected on the lower hemisphere. The P- and T-axes of the input moment tensors are indicated by small stars and diamonds, respectively. The scale below each hemisphere plot shows the relative stress magnitude, defined as $R = (\sigma_1 - \sigma_2) / (\sigma_1 - \sigma_3)$ with uncertainty from bootstrapping in grey.

4. GNSS velocities

The uplift was computed from the GNSS data of the EUREF WG on European Dense Velocities (http://pnac.swisstopo.admin.ch/divers/dens_vel/index.html, Brockmann et al. [2019]). GNSS velocity records are used if there are at least 3 collocated stations and the standard deviation between the solutions for horizontal motion is less than 0.5 mm/a. The uplift is averaged over circular areas (radius 75km) around each lon/lat grid point. Only grid points with a minimum number of 5 observations were considered. Outliers and grid points with large uncertainties were removed. Following Keiding et al. [2015], we compute the spatial derivative of the uplift as a proxy of vertical strain (main text Fig. 12e). To estimate the horizontal strain rate tensor field, the GNSS plate surface velocities were gridded and collected within a radius of 75 km around grid points. A least-square approach was used to estimate the strain rate tensors. Geographical coordinates were transformed to a local Cartesian system centred at each grid point. The resulting maximal shear strain rate is plotted in the main text in Fig. 12f.

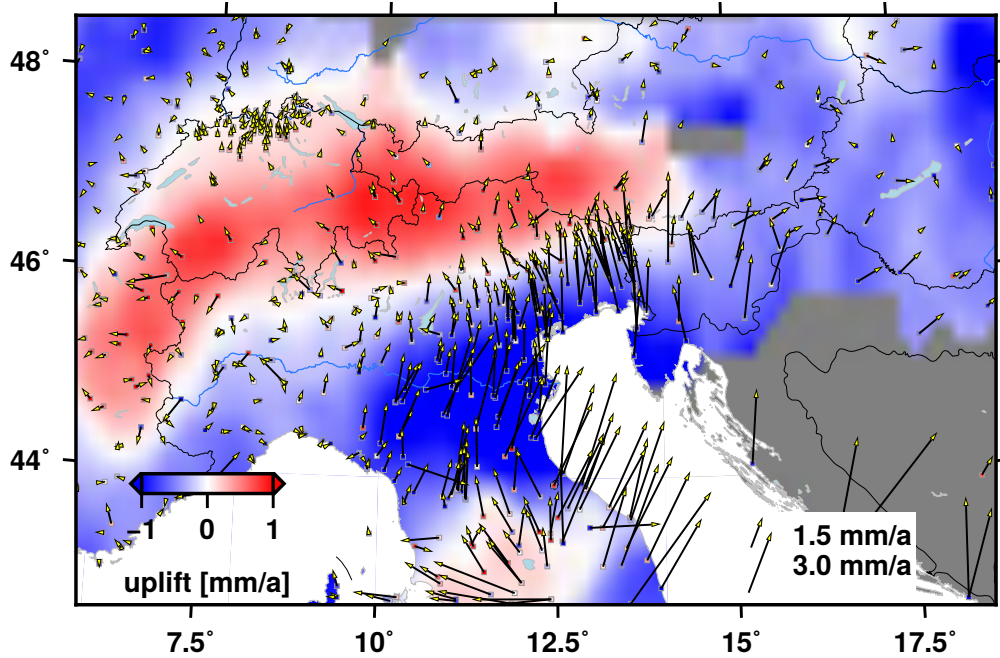


Figure S3: Horizontal GNSS velocities and relative uplift from the European Dense Velocities database (http://pnac.swisstopo.admin.ch/divers/dens_vel/index.html, Brockmann et al. [2019]).

References

- Brockmann, E., Lutz, S., Zurutuza, J., Caporali, A., Lidberg, M., Völksen, C., Sánchez, L., Serpelloni, E., Bitharis, S., Pikridas, C., Fotiou, A., Mathis, E., Sánchez Sobrino, J., Valdés Pères De Vargas, M., Vernant, P., Baron, A., Westerhaus, M., Legrand, J., Kreemer, C., Gianniou, M., Nykiel, G., Figurski, M., Kenyeres, A., and Kurt, A.: Towards a Dense Velocity Field in Europe as a basis for Maintaining the European Reference Frame., 27th IUGG Assembly, Montreal, 2019.
- Cesca, S., Grigoli, F., Heimann, S., Dahm, T., Kriegerowski, M., Sobiesiak, M., Tassara, C., and Olcay, M.: The Mw 8.1 2014 Iquique, Chile, seismic sequence: a tale of foreshocks and aftershocks, *Geophysical Journal International*, 204, 1766–1780, 2016.
- Gephart, J. W. and Forsyth, D. W.: An improved method for determining the regional stress tensor using earthquake focal mechanism data: application to the San Fernando earthquake sequence, *Journal of Geophysical Research: Solid Earth*, 89, 9305–9320, 1984.
- Keiding, M., Kreemer, C., Lindholm, C., Gradmann, S., Olesen, O., and Kierulf, H.: A comparison of strain rates and seismicity for Fennoscandia: depth dependency of deformation from glacial isostatic adjustment, *Geophysical Journal International*, 202, 1021–1028, doi:10.1093/gji/ggv207, 2015.
- Pedregosa, F., Varoquaux, G., Gramfort, A., Michel, V., Thirion, B., Grisel, O., Blondel, M., Prettenhofer, P., Weiss, R., Dubourg, V., Vanderplas, J., Passos, A., Cournapeau, D., Brucher, M., Perrot, M., and Duchesnay, E.: Scikit-learn: Machine Learning in Python, *Journal of Machine Learning Research*, 12, 2825–2830, 2011.